THESIS FOR THE DEGREE OF LICENTIATE OF ENGINEERING

Hydrogen embrittlement in stainless steel 321

Influence of temperature, loading mode and cyclic pre-deformation

VISHNU ANILKUMAR

CHALMERS

Department of Industrial and Materials Science
CHALMERS UNIVERSITY OF TECHNOLOGY
Gothenburg, Sweden 2025

Hydrogen embrittlement in stainless steel 321
Influence of temperature, loading mode and cyclic pre-deformation

VISHNU ANILKUMAR

Technical report no IMS-2025-12

Licentiate Thesis at Chalmers University of Technology
Department of Industrial and Materials Science
Chalmers University of Technology
SE-412 96 Gothenburg
Sweden
Tel: +46 (0)31 772 1000

Printed by Chalmers Digitaltryck
Gothenburg, Sweden 2025

Hydrogen embrittlement in stainless steel 321

Influence of temperature, loading mode and cyclic pre-deformation

VISHNU ANILKUMAR
Department of Industrial and Materials Science
Chalmers University of Technology

Abstract

Driven by the shift towards clean energy, industrial gas turbines engineered for operation with natural gas are increasingly being adapted to operate on hydrogen-natural gas blends or even pure hydrogen. However, the use of hydrogen introduces concerns related to its absorption into structural components, such as fuel supply pipes. Austenitic stainless steel AISI 321, widely used for this purpose, is susceptible to hydrogen embrittlement, a degradation phenomenon due to hydrogen uptake that may result in premature failure. This thesis investigates the influence of temperature, loading mode, and cyclic pre-deformation on hydrogen embrittlement in AISI 321 stainless steel.

In the first part, the influence of temperature and loading mode on hydrogen embrittlement susceptibility is examined. Slow strain rate tensile tests (1×10^{-5} 1/s) at 150°C in gaseous hydrogen showed no signs of embrittlement, whereas strain-controlled low-cycle fatigue tests exhibited significant embrittlement at 120°C. Although deformation-induced martensite was absent at elevated temperatures in both loading modes, fracture analysis of fatigued specimens revealed cracking along δ-ferrite phase boundaries. Further insight from controlled electron channelling contrast imaging (cECCI) of fatigue specimens tested at 120°C revealed strain localization near these boundaries. This suggests that localized deformation, when combined with the presence of hydrogen, could play more critical role in fatigue by promoting crack initiation and propagation. In contrast, tensile failure requires widespread embrittlement (e.g., through martensite formation) to embrittle a larger cross-sectional area. This was observed in tensile specimens tested in hydrogen at room temperature, where cleavage fracture and δ-ferrite cracking occurred. The second part explores the influence of deformation history on hydrogen embrittlement through cyclic pre-deformation. Specimens were subjected to strain-controlled cyclic pre-deformation (100 cycles) across different strain amplitudes. At all strain amplitudes tested, dislocation cells and slip/shear bands were observed. Minimal martensite was present at the highest strain amplitude of 0.6%. Regardless of pre-cycling, hydrogen pre-charging lowered the tolerable plastic strain range at all strain amplitudes. A re-hardening was observed in pre-cycled test bars due to thermal exposure from hydrogen pre-charging or reference exposure in air. Despite this, low-cycle fatigue (LCF) life of these pre-cycled test bars remained comparable to that of non-pre-cycled test bars, with and without hydrogen pre-charging. This finding supports the use of simplified testing procedures where hydrogen charging before LCF loading is performed as a practical approximation of service conditions involving continuous hydrogen exposure during cyclic loading with prolonged hold times, like that of a gas turbine.

Keywords: Hydrogen embrittlement, Austenitic stainless steel, Delta-ferrite, Deformation history, Low-cycle fatigue, Slow strain rate tensile testing.

Preface

The work presented in this licentiate thesis was conducted at the Department of Industrial and Materials Science, Chalmers University of Technology. The research was carried out in the frame of the competence centre TechForH2, with Prof. Emmy Yu Cao as the main supervisor, Prof. Johan Ahlström as co-supervisor, and Prof. Lars Nyborg as the examiner. Industrial supervision was provided by Dr. Frans Palmert, Siemens Energy AB, Sweden. The author acknowledges the funding from the Swedish Energy Agency (P2021-90268) and the TechForH2 member companies: AB Volvo, Scania CV AB, Siemens Energy AB, GKN Aerospace Sweden AB, PowerCell AB, Oxeon AB, RISE, Stena Rederier AB, Johnson Matthey AB and Insplorion AB.

List of appended papers:

Paper 1: **Hydrogen embrittlement at elevated temperature during low cycle fatigue of AISI 321 stainless steel**
Vishnu Anilkumar, Stefan Wanjura, Dirk Kulawinski, Frans Palmert, Johan Ahlström, Lars Nyborg, Yu Cao
Submitted to journal publication

Paper 2: **Hydrogen embrittlement behaviour of AISI 321 stainless steel: Influence of temperature in tensile testing**
Vishnu Anilkumar, Stefan Wanjura, Dirk Kulawinski, Frans Palmert, Johan Ahlström, Lars Nyborg, Yu Cao
To be submitted for journal publication

Paper 3: **Role of cyclic pre-deformation in hydrogen embrittlement behaviour of AISI 321 stainless steel under low cycle fatigue**
Vishnu Anilkumar, Frans Palmert, Daniel Gren, Johan Ahlström, Lars Nyborg, Yu Cao
Manuscript

Contribution to the appended papers:

Paper 1: Siemens Energy executed the fatigue testing in hydrogen gas. The author performed all the experimental characterization and analysis, and drafted the manuscript, which was then revised in collaboration with the co-authors.

Paper 2: Siemens Energy executed the tensile testing in hydrogen gas. The author performed all the experimental characterization and analysis, and drafted the manuscript, which was then revised in collaboration with the co-authors.

Paper 3: The author planned and executed all the experimental characterization and analysis along with Siemens Energy. The author drafted the manuscript, which was then revised in collaboration with the co-authors.

List of acronyms and abbreviations

AISI – American Iron and Steel Institute

ASTM – American Society for Testing and Materials

BCT – Body-Centered Tetragonal

BCC – Body-Centered Cubic

cECCI – Controlled Electron Channelling Contrast Imaging

c – Fatigue ductility exponent

CO_2 – Carbon dioxide

δ-ferrite – Delta Ferrite

DIM – Deformation-Induced Martensite

EBSD – Electron Backscatter Diffraction

ECCI – Electron Channelling Contrast Imaging

FEG-SEM – Field Emission Gun Scanning Electron Microscope

FCC – Face-Centered Cubic

$G_{\alpha'}$ – Gibb's Free Energy of Martensite

G_{γ} – Gibb's Free Energy of Austenite

H – Atomic hydrogen

H_2 – Hydrogen gas

HE – Hydrogen Embrittlement

HEE – Hydrogen Environment Embrittlement

LCF – Low-Cycle Fatigue

M_d – Maximum Temperature for Deformation-Induced Martensite Transformation

M_s – Martensite Start Temperature

N – Cycles to Crack Initiation

NO_x – Nitrogen Oxides

p – Partial Pressure

ppm – Parts Per Million

RA – Reduction of Area

RRA – Relative Reduction of Area

R – Universal Gas Constant

S – Solubility

S_0 – Solubility Constant

SO_x – Sulphur Oxides

SSR – Slow Strain Rate

T – Temperature

TDS – Thermal Desorption Spectroscopy

Ti(C,N) – Titanium Carbonitride

TRIP – Transformation-Induced Plasticity

ΔH – Heat of Solution

ϵ_p : Plastic strain

ϵ'_f : Fatigue ductility coefficient

Table of content

1 Introduction 1
2 Hydrogen embrittlement 3
3 Austenitic stainless steels 5
3.1 Metastability in austenitic stainless steels 5
3.2 Influence of metastability on hydrogen embrittlement 7
4 Influencing factors in the assessment of hydrogen embrittlement 9
4.1 Hydrogen charging 9
4.2 Mechanical loading mode 10
4.2.1 Tensile testing 10
4.2.2 Fatigue testing 11
4.3 Temperature 12
4.4 Pre-deformation 13
5 Methodology 15
5.1 Material specifications and test bar geometry 15
5.2 Hydrogen charging and mechanical testing 15
5.2.1 Grade 1 15
5.2.2 Grade 2 16
5.3 Sample preparation 16
5.3.1 Fracture surfaces 16
5.3.2 Microstructural analysis 17
5.4 Scanning electron microscopy 17
5.4.1 Imaging and chemical analysis in SEM 17
5.4.2 Electron backscatter diffraction 18
6 Summary of appended papers 19
Impact of loading mode and temperature (Paper 1 & 2) 19
Effect of cyclic pre-deformation (Paper 3) 22
7 Conclusions 27
Future Work 29
Acknowledgements 31
References 33

1 Introduction

Industrial gas turbines are widely used for power generation due to their high efficiency, low nitrogen oxide (NO_x) and sulphur oxide (SO_x) emissions, and fuel flexibility [1]. Converting these turbines into hybrid systems offers a practical solution for reducing CO_2 emissions by integrating zero-carbon fuels, such as hydrogen (H_2), to be used alongside natural gas. In these systems, AISI 321 stainless steel is commonly used for fuel supply pipes, combustor parts, and exhaust manifolds due to its high temperature corrosion resistance and weldability [2].

However, the introduction of hydrogen poses challenges to the mechanical integrity of these parts due to hydrogen embrittlement (HE), a degradation mechanism that reduces the ductility of susceptible alloys [3]. AISI 321 is known to be susceptible to HE [4]. Evaluating its performance under conditions relevant to gas turbine operation is critical to determine whether the alloy remain viable or requires replacement.

This is particularly important since a typical gas turbine operating cycle involves start-up and shutdown cycles, as well as prolonged steady-state operation. It is the start/stop cycling that often limits lifespan of components like fuel supply pipes due to the large strain range reversals [5]. These loading conditions necessitates the identification of key microstructural factors and testing conditions that influence HE susceptibility.

This thesis aims to address factors affecting HE in AISI 321 stainless steel through two research questions:

Research question 1: How do temperature and loading mode affect hydrogen embrittlement in AISI 321 stainless steel?

Slow strain rate (SSR) tensile testing is a standard practice for screening materials to evaluate their HE susceptibility; however, the start/stop cycles of gas turbines impose large strain reversals that falls within the low-cycle fatigue (LCF) regime. Therefore, comparing these two loading modes at different temperatures is essential for selecting an appropriate testing methodology. This is particularly relevant because fuel supply pipes are exposed to elevated temperatures (~150 - 200°C), where HE behaviour may differ significantly from that at room temperature.

The importance of research question 1 arises from the metastable nature of stainless steels such as AISI 304 and AISI 321. In these steels, HE susceptibility is closely linked to the formation of deformation-induced martensite (DIM) and the presence of delta-ferrite (δ-ferrite). Both phases, with their body-centered tetragonal (BCT)/ body-centered cubic (BCC) crystal structures, exhibit higher hydrogen diffusivity and lower solubility than the austenitic matrix. This promotes hydrogen accumulation along the interfaces and increases the likelihood of crack initiation and propagation [6–10]. Most HE studies have been conducted at room temperature, where DIM formation is favoured. At this temperature, the co-existence of δ-ferrite and DIM typically leads to premature failure [11]. However, above the M_d temperature which is the threshold temperature, DIM formation is not feasible, and stable austenite correlates with improved HE resistance in tensile tests [12–14]. Whether this improvement also

extends to strain-controlled LCF life remains less known. To address this, the present study performs strain-controlled LCF tests and complementary SSR tensile tests at elevated temperatures where DIM formation is unlikely.

Research question 2: Is the sequence of plastic deformation and hydrogen pre-charging affecting hydrogen embrittlement susceptibility in AISI 321 stainless steel?

In service, turbine components are continuously exposed to hydrogen during cyclic loading and prolonged hold periods. Accurately replicating these conditions through mechanical testing is often complex and time-consuming, and its value is limited without accounting for changes in temperature and slower strain rates experienced in actual turbine operation. As a simplified approach, this study explores the use of cyclic pre-deformation followed by thermal hydrogen pre-charging to evaluate whether deformation history influences susceptibility to hydrogen embrittlement under conditions approaching hydrogen saturation.

The use of cyclic pre-deformation over monotonic tensile pre-straining is to develop a more representative microstructure as a result of strain reversals imposed during gas turbine start/stop cycling. Although tensile pre-straining has been used for studying the influence of pre-deformed microstructures on HE [15,16], the effects of cyclic pre-deformation, which encompasses the primary cyclic hardening regime, remain poorly understood in terms of its impact on remaining fatigue life after hydrogen charging. This stage is expected to produce a microstructure distinct from that generated by monotonic straining, characterized by the development of dislocation cells, and the potential formation of DIM, and deformation twins.

The aim is to determine whether pre-deformation must be considered in conditions approaching hydrogen saturation prior to LCF. If no significant effect is observed, this would support the use of simplified test procedures that omit pre-deformation, while still approximating relevant conditions involving continuous hydrogen exposure during cyclic loading and hold periods.

2 Hydrogen embrittlement

Exposure of metallic materials to H_2 environments often results in hydrogen uptake. Atomic hydrogen (H) enters the metal from gas phase through chemisorption, where dissociated hydrogen atoms from H_2 molecules adsorb onto metal surface, forming hydrogen-metal bonds by means of electron sharing. Atomic H can then diffuse into the metal paving the way for hydrogen entry [17]. This process often results in the deterioration of ductility in susceptible alloys through a phenomenon known as hydrogen embrittlement (HE). Hydrogen embrittlement was first reported in 1874, substantial loses in fracture strain of steel and pure iron was observed after immersion in hydrogen-containing solutions (sulphuric acid and hydrochloric acid) [18]. The subsequent low temperature heat treatment led to hydrogen desorption which resulted in the restoration of ductility, underlining the effect of hydrogen uptake.

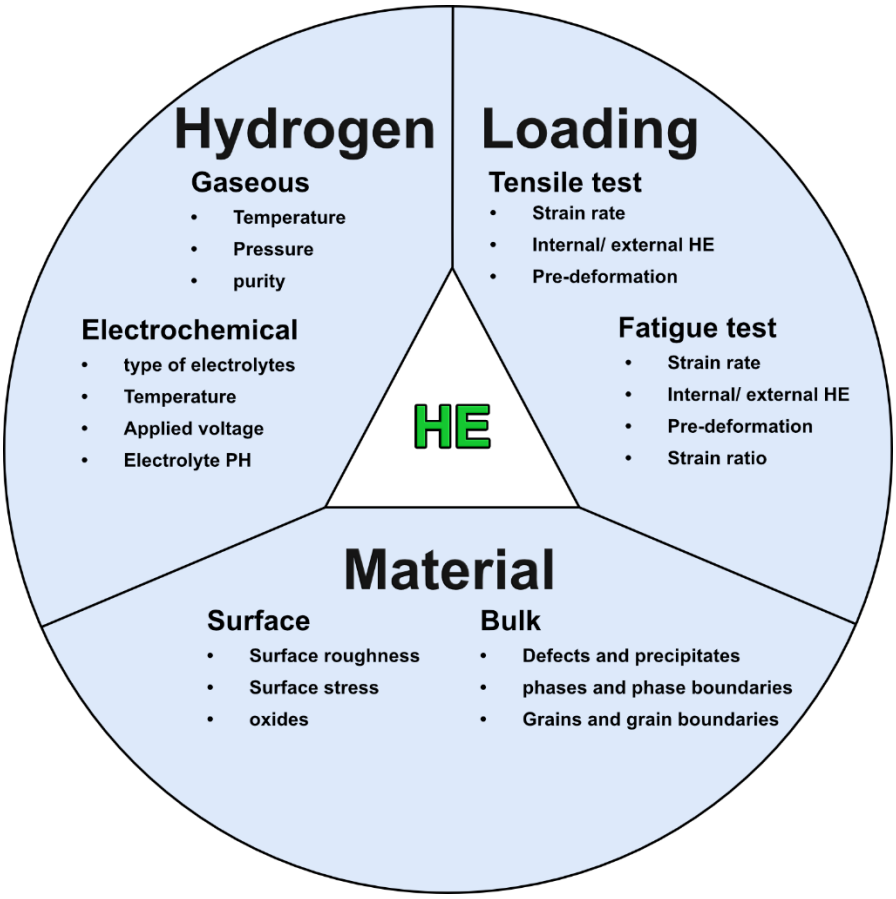

Fig. 1. Schematic illustration of nature of HE and the influencing factors, redrawn from [3].

Figure 1illustrates schematically the nature of HE and the influencing factors. The complex nature of HE arises from the interplay between three primary factors: (i) the type of mechanical loading, (ii) hydrogen environment, and (iii) materials. These factors jointly make it an open research area of interest. In recent years, there is an increased drive towards establishing mechanical test facilities for handling pressurized hydrogen gas at high temperatures and hydrogen quantification techniques like thermal desorption spectroscopy (TDS). This is especially important considering the growing interest in industries, as they are aiming to lower

carbon emissions in power generation, transportation, and steel manufacturing. Therefore, it is crucial to identify critical parameters influencing HE in the target application, rather than solely rely on general embrittlement indexes found from literature. The following sections will briefly cover different influencing factors on assessing HE in relation to the scope of this work.

3 Austenitic stainless steels

Austenitic stainless steels (Cr-Ni-300-series) are iron-based alloys with austenite having face-centred cubic (FCC) crystal structure as primary phase. They are renowned for their excellent corrosion resistance and mechanical properties, and thus finds use in numerous applications ranging from food processing to hydrogen production, storage and transport [19,20]. The phase stability of austenite against formation of martensite and δ ferrite is crucial for HE resistance. This section examines the factors that influence austenite stability in austenitic stainless steels and explores how reduced austenite stability compromises the HE resistance.

3.1 Metastability in austenitic stainless steels

Alloying elements and processing conditions such as cooling rate and heat treatment play critical roles in determining the phase stability of austenite, particularly its transformation to DIM (BCT, commonly simplified as BCC) or δ-ferrite (BCC ferrite). The influence of austenite (nickel, carbon, manganese etc.) and ferrite (chromium, molybdenum, silicon etc.) stabilizing elements respectively, is often assessed using the concepts of nickel equivalent (Ni_{eq}) and chromium equivalent (Cr_{eq}) values. Since the formation of δ-ferrite or martensite cannot be reliably predicted using equilibrium phase diagrams, the Schaeffler diagram is typically employed. This diagram predicts the phases present at room temperature following rapid cooling from the solution treatment temperature, based on the calculated Ni_{eq} and Cr_{eq} values [21]. A schematic of Schaeffler diagram with the position of alloys investigated in the present study is shown in Fig. 2. Here the difference in the chemical composition of grade 1 and grade 2 AISI 321 stainless steel used for the study results in a difference in predicted δ-ferrite content.

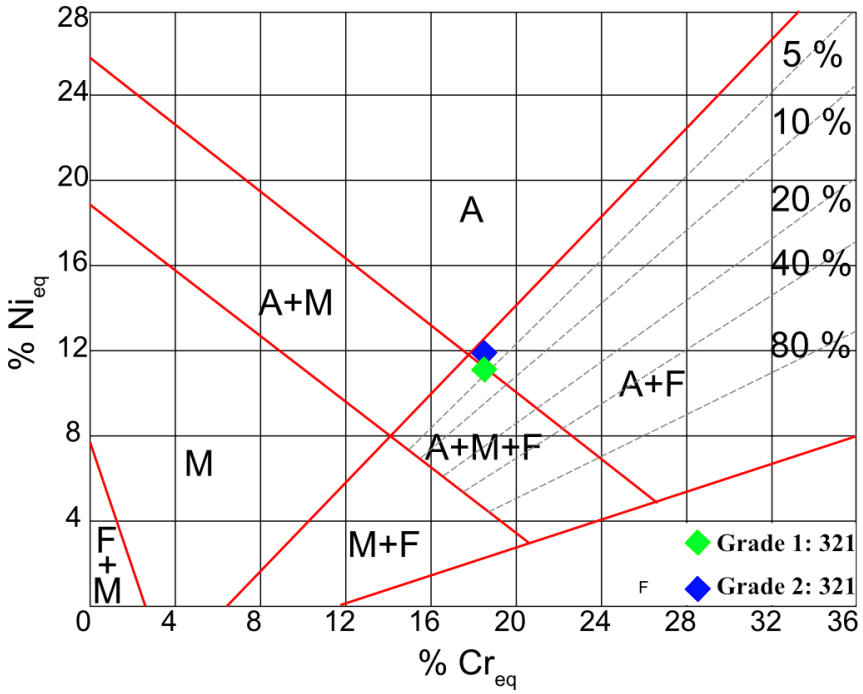

Fig. 2. Schaeffler diagram. Austenite, ferrite, and martensite is abbreviated as A, F, and M respectively; The two AISI 321 grades used in the present study are marked. Ni_{eq} = Ni + (30 x C) + (0.5 x Mn); Cr_{eq} = Cr + Mo + (1.5 x Si) + (0.5 x Nb); The percentages marked towards right hand side corner of the plot indicates the fraction of phased expected.

A small amount of δ-ferrite can be present in austenitic stainless steels with relatively low nickel content. Depending on the chemical composition, δ-ferrite formed during solidification may persist in the microstructure even after thermomechanical processing and solution heat treatment, remaining stable at ambient temperature. Even though its formation hinders a complete austenitic microstructure, the retention of δ-ferrite is not always considered to be a demerit. When cast-ingot composition is tailored to have typically (1 – 6)% δ-ferrite, the chance of cracking is reduced during forging or hot working [22]. A few percent δ-ferrite in solution annealed state is also beneficial for improved weldability in austenitic stainless steels, as this helps in suppressing hot cracking [23].

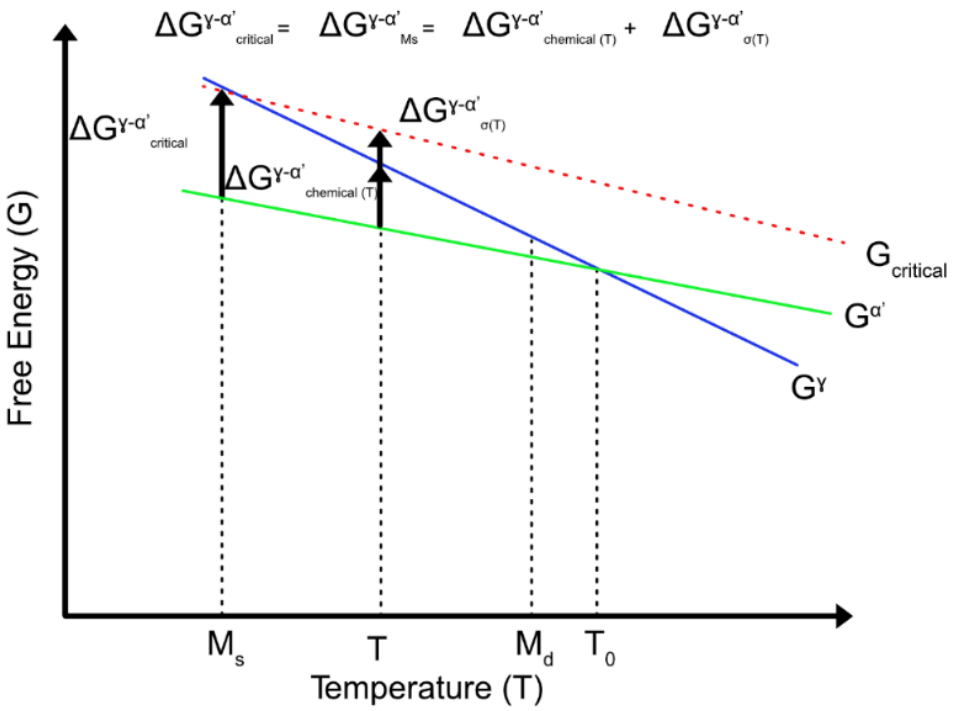

Fig. 3. Schematic portraying thermodynamics of austenite to martensite transformation. Redrawn with permission from [12].

Additionally, austenitic stainless steels with low nickel content exhibit tendency for austenite to martensite transformation upon deformation, which is temperature dependent. To understand the influence of temperature on this transformation, it is essential to examine the underlying thermodynamics. The Gibb's free energy curves of austenite (G_{γ}) and martensite ($G_{\alpha'}$) are plotted against temperature (T) schematically in Fig. 3. At temperatures below T_0, martensite formation is thermodynamically favourable as its free energy is lower than that of austenite. However, the transformation becomes feasible only when sufficient undercooling occurs, which is achieved at the martensite start temperature (M_s). This is required to overcome the activation energy barrier associated with creating a new austenite-martensite interface and accommodating the associated elastic strain energy.

At M_s, the free energy difference reaches a critical value ($\Delta G_{\gamma\text{-}\alpha' \text{critical}}$), representing the minimum energy needed for the spontaneous transformation of austenite into martensite. Between M_s and T_o, spontaneous transformation is hindered because the chemical free energy difference ($\Delta G_{\gamma\text{-}\alpha' \text{chemical}}$) is less than $\Delta G_{\gamma\text{-}\alpha' \text{critical}}$. At a given temperature T in this range, external

energy must be supplied to enable the transformation. This can be achieved through applied stress, which contributes an additional term ($\Delta G_{\gamma\text{-}\alpha'\sigma(T)}$) to the total free energy, compensating for the insufficient chemical driving force. As the deformation temperature increases further, $\Delta G_{\gamma\text{-}\alpha'\text{chemical}}$ continues to decrease, eventually reaching a point where even with applied stress, transformation to martensite is not possible. This temperature is defined as the M_d temperature. In the temperature range between M_d and T_0, the chemical driving force is insufficient to initiate the transformation, and deformation occurs preferentially in the austenitic phase [12].

Hence, variants of austenitic stainless steels where austenite deformation leads to martensite formation, are termed as metastable austenitic stainless steels, while stainless steels having higher austenite stability against deformation-induced martensite, such as 316L with higher Ni_{eq} is referred to as stable austenitic stainless steels. Among 300-series, 301, 304, 321 grades etc. belong to the class of metastable austenitic stainless steels [12]. These types are known for their substantial strain hardening rate and large necking strain due to transformation induced plasticity (TRIP) phenomenon which is activated during deformation. The metastable nature of these alloys plays a major role for the TRIP effect [12,24,25].

AISI 321 stainless steel is a variant of austenitic stainless steel AISI 304, where added titanium (Ti) precipitates to TiC. The consequently reduced availability of carbon in austenite hinders $M_{23}C_6$ precipitation and improves resistance towards intergranular stress corrosion cracking, when heated to its carbide precipitation range (425°C-850°C). This property of AISI 321 makes it applicable in structural components, high-temperature components of nuclear power plants, and, like in the present study fuel supply pipes, combustor parts, and exhaust manifolds of gas turbines [2,20]. As mentioned in the preceding paragraph, AISI 321 undergoes a TRIP effect, which is generally advantageous for metals forming. However, it is generally accepted that deformation-induced martensite which causes TRIP effect is detrimental to HE resistance of AISI 321. For the use of AISI 321 in H_2-rich environments, HE is deleterious to the mechanical integrity. In the following subsections the impact of DIM and δ-ferrite on HE susceptibility of metastable austenitic stainless steels are discussed briefly.

3.2 Influence of metastability on hydrogen embrittlement

The diffusion rate of hydrogen and its solubility in phase(s) present in the material governs its susceptibility to HE. It is the diffusible hydrogen that deteriorates the HE resistance, and thus the rate of diffusion is an important parameter in judging the ability of hydrogen to migrate to the crack fronts. The diffusion coefficient (D) of hydrogen in BCC structural high purity ferritic steels with low hydrogen solubility is about ~ 5.8 x 10^{-8} m^2/s at 298K. These steels are often under risk of HE. For FCC structured austenitic steels, solubility of hydrogen is high, while diffusivities are relatively low with D of ~ 7.4 x 10^{-16} m^2/s at 298K; the value is subject to variation as the diffusion process is sensitive to changes in alloy chemistry. Therefore, austenitic steels are for most cases preferred candidates for hydrogen exposed environments [26].

In metastable grades like AISI 321 and AISI 304, the formation of deformation-induced martensite with a BCT or BCC structure is inevitable at ambient temperatures. Due to the relatively low content of interstitials in stainless steels, this structure is commonly referred to

as BCC rather than BCT [27]. The formation of martensite from hydrogen saturated austenite leads to accumulation of hydrogen along the phase boundaries between austenite and martensite. This worsens the interface strength and allows its decohesion, causing HE. This phenomenon is well known from laboratory testing over the years, where martensite transformation has been correlated to decrease in tensile ductility [6,9,28–31]. It is also reported that fatigue crack propagation is accelerated in the presence of hydrogen, where martensite formation at the crack tip provides hydrogen diffusion pathways and can accelerate crack propagation [10,32,33]. A similar effect of fast diffusion of hydrogen is possible in δ-ferrite due to its BCC structure. This may reduce tensile ductility and stress-controlled low-cycle fatigue life [8,11,34]. At temperatures that favour the formation of martensite, both martensite and δ-ferrite could worsen the HE resistance of the alloy when assessed using tensile testing or fatigue loading.

4 Influencing factors in the assessment of hydrogen embrittlement

Assessing hydrogen embrittlement susceptibility of a material involves several factors, including the hydrogen charging method, microstructural condition, mechanical testing approach and temperature. This complexity is illustrated in Fig. 1. In AISI 321, these parameters significantly influence HE evaluation. To ensure reliable performance in hydrogen environments, careful selection of these factors is essential for studying HE. This section outlines the most relevant considerations.

4.1 Hydrogen charging

Hydrogen charging is a process of artificially introducing hydrogen into the material under controlled conditions for subsequent testing or quantification. Hydrogen charging can be performed either using an electrochemical setup or an autoclave. In electrochemical hydrogen charging the sample acts as a cathode, where a hydrogen evolution reaction takes place. The limitation of such a setup is the low temperature achievable due to the nature of the electrolyte (distilled water with boiling point around 100°C). In practice, the achievable temperature with acceptable evaporation rates would be around 80°C to 90°C, at a pressure of 1 atm. This is a challenge especially when hydrogen charging austenitic stainless steels. This is because the low diffusivities of hydrogen in austenite leads to steeper H concentration gradient (Fig. 4a), leading to an embrittled surface layer and a ductile interior (under tensile testing) which can be partially or not affected by hydrogen in most cases (Fig. 4b). Additionally, the supersaturation of hydrogen in this thin layer can be detrimental in case of metastable stainless steels like AISI 321. Figure 5 shows martensite transformation associated with electrochemical hydrogen charging (Fig. 5a) along with surface cracks (Fig. 5b). This can occur based on the electrolyte (acidic or alkaline) and charging parameters of choice such as applied current (Ampere), temperature, which if not carefully selected will affect assessing HE.

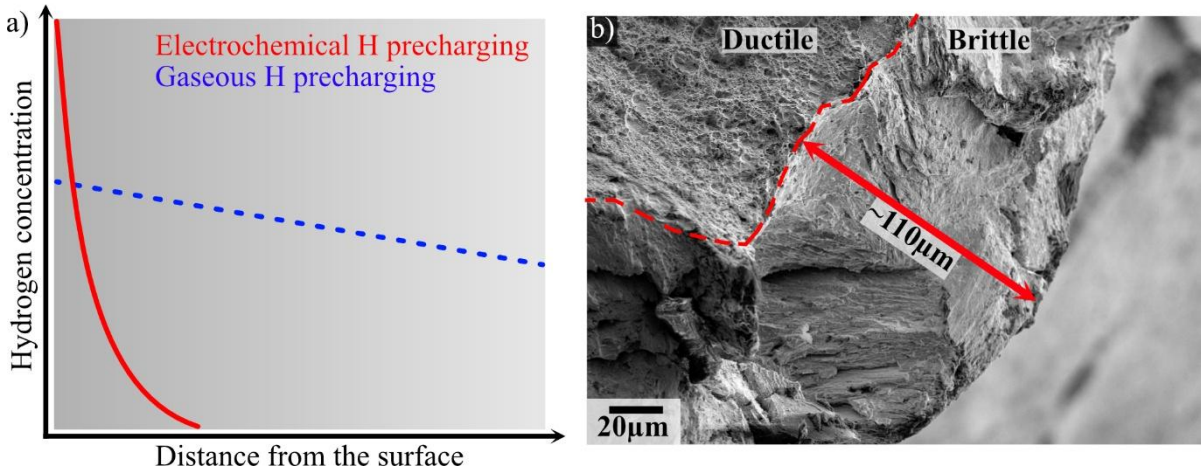

Fig. 4. (a) schematic illustration of hydrogen concentration profile developed due to pre-charging technique as a function of distance from the surface; (b) Surface embrittled zone in AISI 321 after electrochemical hydrogen charging and tensile testing using strain rate of 1 x 10^{-4} 1/s.

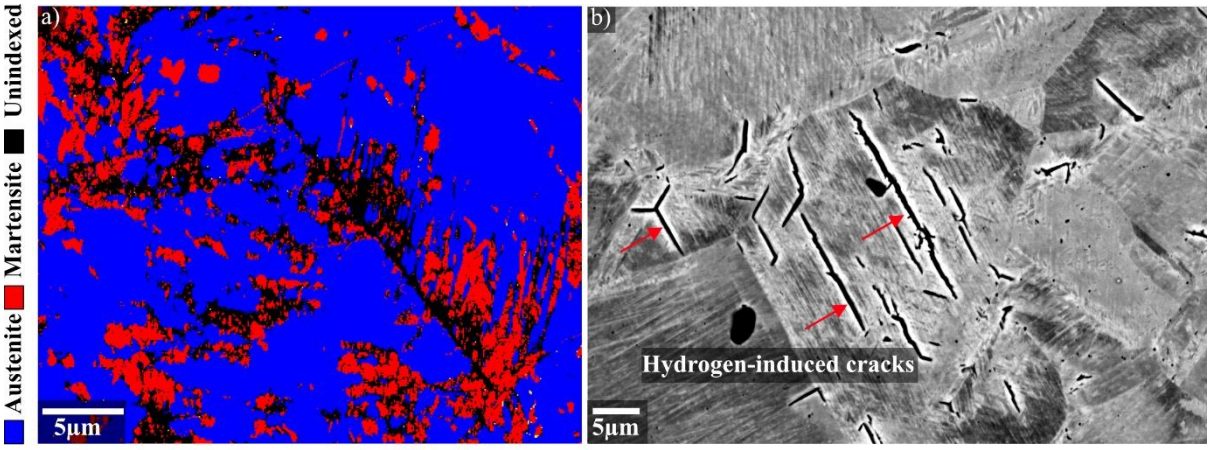

Fig. 5. Electrochemical hydrogen charging induced damage (a) martensite transformation (b) surface cracking.

An alternative is to use gaseous hydrogen charging at high temperature and under pressure in an autoclave to facilitate hydrogen uptake, as in the present study. The high temperature helps in decreasing the hydrogen concentration gradient and ensures a relatively uniform distribution of hydrogen in comparison to electrochemical hydrogen charging, as schematically shown in Fig. 4a. In addition, an increase in partial pressure of hydrogen gas will increase the solubility of hydrogen in the metal. This is explained by Sievert's law expressed in equation (1), where S_0 is the solubility constant, p is the partial pressure, ΔH is the heat of solution, R is the universal gas constant, and T is the absolute temperature in degrees Kelvin.

$$S = S_0 . \sqrt{p} . e^{\frac{-\Delta H}{RT}} \quad (1)$$

The solubility (S) depends on the square root of partial pressure (p) [35]. Thus, in certain material, the use of gaseous hydrogen charging allows producing varying hydrogen concentration and its distribution depending on the careful selection of temperature, pressure, and time.

4.2 Mechanical loading mode

Testing is important to evaluate HE sensitivity of materials. A plethora of testing methods exist and can be adopted in H_2 environments. In this section, a brief introduction to two testing methods used for this study, tensile testing and fatigue testing is provided in context to HE.

4.2.1 Tensile testing

Tensile testing involves straining of a test specimen in tension at a constant rate either using an extensometer or by a constant cross head displacement equivalent to a desired strain rate along the gage. The test can be run until fracture, and the data from the test is used to identify properties such as yield strength, strain hardening, ultimate tensile strength, ductility etc.

The test procedure for evaluating hydrogen embrittlement (HE) is based on ASTM standards G129-21 and G142-98 (reapproved in 2016), which are widely used as material screening methods for assessing HE susceptibility. Slow strain rate (SSR) testing is preferred because it enables time-dependent phenomena, such as hydrogen-assisted degradation. At high strain rates, on the other hand, it might be difficult to reach a sufficient high hydrogen content ahead

of crack tips. The fracture may procced without the assistance from H. However, in the reality, the strain rate is supposed to remain sufficiently high to ensure specimen failure within a practical timeframe for evaluation [36]. A detailed approach to tensile testing in H_2 is mentioned in ASTM G142-98 (reapproved in 2016), where an extension rate of 0.002 mm/s ± 10% in the gage is recommended for smooth tensile bars.

Hydrogen embrittlement in tensile testing is typically observed as a reduction in the tensile ductility of the alloy. The reduction of area (RA) measured from smooth specimens is recommended for assessing HE. It is determined from the post-fracture cross-sectional areas. The RA provides a more fundamental measure of ductility than uniform elongation because percentage elongation, commonly measured using an extensometer, can be influenced by the specimen geometry, particularly the ratio of parallel length to gage diameter, leading to variability [37]. The RA value can be used to calculate the relative reduction of area (RRA) using Equation (2), which quantifies the material's resistance to hydrogen embrittlement. An RRA value of '1' indicates that hydrogen has no measurable effect on the macroscopic tensile ductility of the alloy [38].

$$\text{Relative reduction of area (\%)} = \frac{\text{Reduction of area in Hydrogen}}{\text{Reduction of area in Air}} \quad (2)$$

According to this measure, metastable austenitic stainless steels, especially 321 is less resistant to HE at RT, in comparison to stainless steel 316L with higher Ni_{eq}.

4.2.2 Fatigue testing

Many engineering failures in metals subjected to cyclic loading occur due to fatigue. Fatigue failure is not an abrupt or unexpected event. Rather, it is the culmination of a progressive sequence of cyclic deformation leading to damage accumulation over time. In FCC metals, fatigue deformation typically involves several stages: cyclic hardening/softening, cyclic saturation, the evolution of fatigue damage caused by cyclic slip irreversibilities, and finally, the initiation and growth of cracks that lead to failure [39].

Cyclic loading with governed plastic strain leads to shorter lives and is often characteristic of low-cycle fatigue (LCF) testing. In contrast, high-cycle fatigue regime is dominated by elastic strain and results in longer lives. Fatigue testing can be performed in stress-controlled or strain-controlled mode. A strain versus life curve on a logarithmic scale is shown schematically in Fig. 6. These curves are derived from fatigue testing performed under fully reversed (R_ϵ = -1) in strain-control mode with data acquisition of stress in accordance with the ASTM standard no. E606/E606M-21[37]. The plot shows a steeper slope '*c*' for cycles to failure in the LCF regime, while a shallower slope '*b*', indicative of longer lives is seen for high-cycle fatigue regime. A strain-based approach to fatigue considers the localized yielding at areas of stress concentrations within the material, where fatigue cracks usually begin. It provides better estimation for intermediate to short fatigue lives.

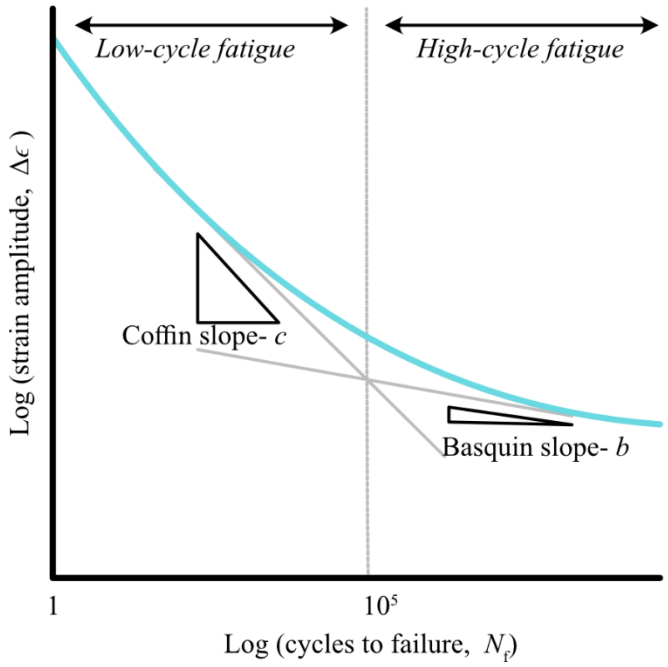

Fig. 6. Schematic of strain amplitude ($\Delta\epsilon$) vs cycles to failure (N_f).

The loss in fatigue life at high strain amplitudes is thus linked to increase in plastic strain amplitude. The Coffin-Manson approach as shown in equation 3 is used to describe this region [40].

$$\Delta\epsilon_p = \epsilon'_f(2N_f)^c \quad (3)$$

Here, $\Delta\epsilon_p$ is the plastic strain amplitude obtained from stable hysteresis loop at half-life, N_f is the number cycles to failure, ϵ'_f and c are the fatigue ductility coefficient and fatigue ductility exponent, which are the intercept and slope of the line fitted on the data and are material properties. Low-cycle fatigue properties of susceptible materials are affected by hydrogen, and manifests as a low N_f. A total strain range (twice the strain amplitude) vs cycles to failure plot can provide quantitative information into severity of HE, here a hydrogen embrittlement will reduce the tolerable inelastic strain range at any given number of cycles to failure, and a lower ϵ'_f is usually seen. According to ASTM standard no. E606/E606M-21, there are no restrictions on the environmental factors such as temperature, medium, humidity, pressure, provided they are controlled during testing.

4.3 Temperature

Hydrogen embrittlement is temperature-dependent, with its severity peaking near or below room temperature and diminishing at both lower and higher temperatures. Impact of temperature on hydrogen environment embrittlement (HEE) is shown in Fig. 7. The HEE index refers to embrittlement of alloys when tested in the presence of hydrogen. Most austenitic stainless steels are found to be susceptible to HE in the temperature range of -150°C to +150°C. An explanation to this temperature dependence is the trapping of hydrogen within the material. When all traps are occupied with hydrogen, a minimum in HEE index is obtained.

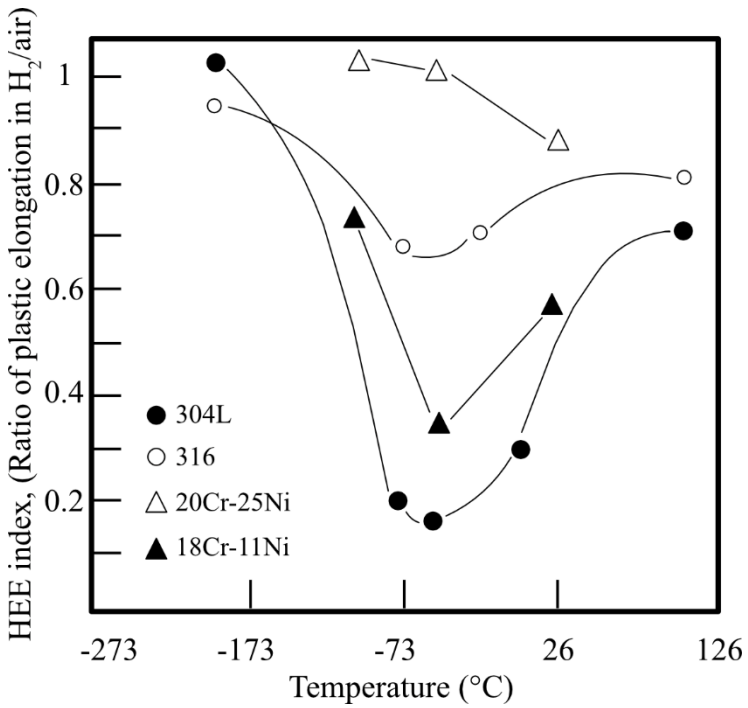

Fig. 7. Impact of temperature on hydrogen environment embrittlement (HEE), for selected steels [14].

At low temperatures diffusion is too sluggish to sufficiently fill traps, while enhanced mobility of hydrogen at higher temperatures prevents sufficient trapping [41]. Traps referred here are microstructural features that interact with hydrogen, and that are non-beneficial in preventing HE.

Tensile testing is an accelerated method to access the HE susceptibility of alloys. However, in applications like gas turbines where components experience large strain reversals, the loading mode falls within LCF regime. Therefore, it is essential to determine whether the influence of temperature on HE observed in tensile tests holds true under cyclic loading conditions. Studies on superalloys, such as Inconel 718, indicate that HE effects in LCF follow a similar temperature-dependent trend as seen in monotonic testing, with HE peaking near room temperature and diminishing at high temperature [42]. These findings suggest a correlation between tensile and LCF data, although the magnitude of HE effects in LCF tends to be more conservative. However, there is limited data available on the effects of temperature and mechanical loading modes on hydrogen embrittlement in metastable austenitic stainless steels. Understanding the dependence of HE on temperature and loading mode, particularly the differences between SSR testing and LCF, is crucial. This is especially important within the narrow temperature window (-150°C to 150°C) in which HE is known to occur in these alloys.

4.4 Pre-deformation

Hydrogen embrittlement sensitivity is strongly influenced by a material's initial microstructure. The effects of pre-deformation introduced through processing methods such as cold working, machining, or controlled tensile straining on HE have been reported [7,15,16,43]. In austenitic stainless steel like AISI 316L, which is more stable against DIM transformation, pre-deformation mainly introduces dislocations, the density and arrangement of which depend on

the level of applied strain [44]. In contrast, metastable austenitic stainless steels such as AISI 321 undergo deformation-induced martensite formation [25].

For example, applying ~10% pre-strain in AISI 304 stainless steel can reduce HE resistance due to increased martensite content [16]. Martensite facilitates hydrogen transport, The resultant accumulation of hydrogen at interfaces leads to subsequent failure. Pre-strained AISI 316L stainless steel, which does not form martensite, exhibits limited sensitivity to HE when precharged with hydrogen. However, its susceptibility increases during in-situ hydrogen environment testing without pre-charging, due to the role of dislocations in enhancing hydrogen transport [44]. In contrast, in alloys with martensite, hydrogen transport and thus HE occurs readily, regardless of whether the hydrogen is introduced by pre-charging or from the test environment [15]. In summary, HE in pre-deformed microstructures are affected by initial microstructural features like martensite and the test methodology used.

5 Methodology

5.1 Material specifications and test bar geometry

Two different grades of austenitic AISI 321 stainless steels in as-received condition were used in this licentiate study. Grade 1 was solution treated at 1050°C for 1 hour followed by air quenching. Grade 2 was solution treated at 1070°C for 2.5 hours and water cooled, followed by stress relieving at 380°C for 8 hours. The chemical composition of the steels is listed in Table 1. For grade 1, the test bars were extracted along the transverse cross-section of a solution annealed hot rolled plate (grade 1) and prepared according to ASTM E8/E8M-22 (gage length of 30 mm and diameter of 6 mm) for tensile testing and ASTM E606/E606M-21 (gage length of 11 mm and diameter of 6 mm) for low-cycle fatigue testing. For grade 2, the test bars were extracted perpendicular to the rolling direction from a solution annealed hot-rolled ring and prepared according to ASTM E606/E606M-21 (gage length of 12.7 mm and diameter of 6.35 mm) for low-cycle fatigue testing. These test bars from grade 2 material were ground using P1000, P1200, P2000, P4000 silicon carbide (SiC) abrasive paper, followed by polishing using diamond suspension of 3 μm and 1 μm, respectively

Table1: Chemical composition of AISI 321 in wt.% used in this study.

Grade	C	Mn	Si	Cu	Ni	Cr	Ti	Co	N	Fe
1	0.04	1.8	0.43	0.44	9.01	17.39	0.29	0.14	0.44	Bal
2	0.04	1.68	0.47	0.19	9.32	17.41	0.32	Nil	0.02	Bal

5.2 Hydrogen charging and mechanical testing

5.2.1 Grade 1

The test bars were thoroughly cleaned in an ultrasonic ethanol bath for 10 minutes to ensure surface cleanliness prior to hydrogen charging. High-purity hydrogen (grade 5.0) was used for the study. To minimize contamination from gases such as oxygen, a hydrogen flushing procedure was implemented. The autoclave was pressurized to 3 MPa, held for 25 minutes, and then depressurized to atmospheric levels. This cycle was repeated five times to ensure a clean hydrogen environment. For hydrogen charging, grade 1 test bars were exposed to H_2 at 350°C and 4.6 MPa for a total duration of 672 hours. After charging, the specimens were gradually cooled to room temperature while still in a hydrogen atmosphere. Once cooled, the test bars were extracted and stored at - 20°C in a commercial-grade refrigerator. Liquid nitrogen storage was avoided to prevent martensitic transformation in the alloy triggered by rapid cooling to lower temperature. To determine total hydrogen concentration, small coupons were extracted from the grips of the test bars and analysed using a Bruker Galileo G8. Hydrogen pre-charging increased the total hydrogen concentration from 3.5 wt.ppm in the as-received condition to 21.5 wt.ppm.

Mechanical testing of grade 1 material was performed in 4.6 MPa hydrogen gas at both room-temperature and elevated temperatures (120°C for LCF and 150°C for tensile testing). LCF testing was run at 120°C to prevent extensometer damage which happened at 150°C. Both

tensile and LCF testing were performed in strain-controlled mode. The strain rates used were 1 x 10^{-5} (1/s) for tensile testing and 1 x 10^{-3} (1/s) for LCF test, respectively. Tensile testing was carried out until fracture. LCF tests were conducted at a total strain amplitude of 0.45%, using a triangular waveform and a strain ratio (R_ε) of - 1. The test was terminated once a prespecified load drop of 20% from peak tensile stress was observed. This was denoted as crack initiation. The number of cycles at this moment was recorded. Following this, the extensometer was removed, and the specimens were fractured in tension close to ambient temperature in air.

5.2.2 Grade 2

Test bars manufactured from grade 2 AISI 321 stainless steel were subjected to cyclic pre-deformation (100 cycles) prior to hydrogen charging at total strain amplitudes of 0.3%, 0.45%, and 0.6% using a triangular waveform with a strain ratio (R_ε) of -1. A constant strain rate of 1 x 10^{-3} (1/s) was used for all tests which were performed in ambient atmosphere. Following pre-cycling, residual strain values were recorded using an extensometer (MTS 2620-603, gage length = 10 mm, travel length = ±1 mm) at zero applied force. A 10-second hold was applied to allow stabilization of the force and strain readings before measurement. The test bars underwent the same ultrasonic cleaning procedure in ethanol prior to hydrogen charging. Thermal hydrogen pre-charging was conducted at 350°C and 5.1 MPa for 672 hours using grade 5.0 hydrogen, with a flushing process consistent with that used for grade 1 specimens. After charging, the specimens were cooled to room temperature under a hydrogen atmosphere, and then stored at - 20°C.

To isolate the effects of thermal exposure, an identical heat treatment (350°C in air for 672 hours) was applied to the pre-cycled reference test bars. For the non-pre-cycled test bars, hydrogen charging was performed simultaneously with the pre-cycled test bars. However, no thermal exposure was applied to the non-pre-cycled reference bars. Fatigue testing of pre-cycled test bars was resumed by offsetting the extensometer to the previously recorded residual strain value. The strain-controlled testing was conducted under identical conditions and continued until fracture. Fatigue tests were also performed on non-pre-cycled test bars, starting from zero strain and zero force, for both hydrogen pre-charged and uncharged conditions. A 5% stress drop was used as the failure criterion during data processing, thus only tests with cracks formed within the extensometer were used for further analysis.

5.3 Sample preparation

5.3.1 Fracture surfaces

After careful transportation from the test rig to the laboratory, the fracture surfaces were stored in a desiccator to avoid exposure to moisture. Before the analysis, the fracture surfaces were ultrasonicated in isopropanol and dried using compressed air to remove dust and other contaminants obscuring fracture surface examination. The samples were then mounted for microscopy analysis on standard SEM stubs. The same procedure was applied for grade 1 and grade 2 specimens.

5.3.2 Microstructural analysis

For microstructural observation of the as-received material from both grade 1 and grade 2 AISI 321 stainless steels, small specimens were extracted along the longitudinal and transverse directions of the test bars. They were hot mounted, then ground using P1000, P1200, P2000, P4000 SiC abrasive papers. These steps were followed by polishing using diamond suspensions of 3 μm and 1 μm, finally 0.05 μm colloidal silica was used.

For post-mortem characterization, the fracture surfaces of grade 1 material were sectioned along the longitudinal axis for tensile specimen and along the fatigue zone in LCF specimen using Buehler Isomet slow speed cutter with a diamond blade. Tensile samples underwent grinding using P1200 SiC abrasive paper, while LCF specimens were avoided from this step due to their small size. Electropolishing using Struers A3 electrolyte was performed at 26 V for 30 seconds (tensile) or 60 seconds (fatigue), followed by ultrasonication in ethanol for 15 minutes. Slow speed cutting and electropolishing was employed to prevent accidental formation of deformation-induced martensite. For grade 2 specimens, pre-cycled microstructure was examined after electropolishing using the same parameters as for grade1, along the gage section. No grinding was applied for this stage as the surfaces of the test bar had been polished to 1 μm. The samples were dried and mounted on stubs using silver paint for further analysis.

5.4 Scanning electron microscopy

Scanning electron microscopy (SEM) analysis was performed using Zeiss Gemini 450 equipped with field emission gun (FEG) source. Specifications of imaging is provided in following sections.

5.4.1 Imaging and chemical analysis in SEM

Secondary electron (SE) and backscattered electron (BSE) detectors were primarily used for imaging. SE imaging, conducted at an accelerating voltage of 5-10 kV and a probe current of 500 pA, was employed to reveal surface topography, particularly on fracture surfaces. BSE imaging, which provides compositional and orientation contrast, was used for microstructural analysis. Controlled electron channelling contrast imaging (cECCI) was performed on grade 1 specimens using the BSE detector at an accelerating voltage of 30 kV and probe current of 5 nA, with a working distance of 8 mm. The procedure involved tilting the specimen to an eucentric position, followed by electron backscatter diffraction (EBSD) mapping of the selected area. The Euler angles of selected grains were input into the TOCA software, which simulated Kikuchi band patterns to suggest appropriate tilt conditions for achieving two-beam diffraction and channelling contrast in the target grain [45].

For grade 2 specimens, electron channelling contrast imaging (ECCI) was performed at an accelerating voltage of 20 kV and probe current of 5 nA, with a working distance of 7 mm. Since site-specific information was not required, cECCI was not employed and two-beam conditions were obtained on random grain orientations. Energy-dispersive spectroscopy (EDS) point analysis was performed near secondary cracks on fracture surfaces using an Oxford

system integrated with the FEG-SEM at an accelerating voltage of 5 kV and probe current of 1.5 nA for 300 seconds per point, with a working distance of 8.5 mm.

5.4.2 Electron backscatter diffraction

Electron backscatter diffraction (EBSD) using the Oxford symmetry system was employed for phase mapping. For tensile specimens, EBSD acquisition was conducted on the cross-section along the longitudinal axis, away from the necked region, using an accelerating voltage of 20 kV and a probe current of 12 nA. An area of 0.12 mm² was mapped with a step size of 0.15 µm. For LCF specimens, EBSD was performed on the external longitudinal surface of the fatigue zone using the same SEM settings, covering an area of 0.3 mm² with a step size of 0.2 µm. A working distance of 8-10 mm was maintained for all acquisitions. For grade 2 specimens, EBSD was acquired at an accelerating voltage of 20 kV and probe current of 12 nA with a finer step size of 0.1 µm. Data analysis was carried out using the open-source MTEX toolbox (version 6.0.0) in MATLAB® [46].

Phase differentiation of δ-ferrite and deformation-induced martensite from the EBSD maps was performed using the 'Classify' tool in Aztec Crystal software. Band contrast images were used to morphologically distinguish δ-ferrite (characterized by its string-like morphology) from martensite. The trained model was then applied to additional datasets, with minor adjustments to the classified regions based on the quality of the band contrast images.

6 Summary of appended papers

This section summarizes the key findings of the appended papers.

Paper 1 investigates the effect of temperature on hydrogen embrittlement under low-cycle fatigue and Paper 2 examines the same during tensile testing. Together, these two papers provide insights into the influence of loading mode on HE at different temperatures. The effect of cyclic pre-deformation on hydrogen embrittlement is the focus of Paper 3.

Impact of loading mode and temperature (Paper 1 & 2)

The studies focussing on objective 1 were carried out on AISI 321 stainless steel (composition in Section 5.1) with grade 1 under identical hydrogen pressure and purity. Papers 1 and 2 show that temperature dependent HE is influenced by loading mode and microstructure. The presence of δ-ferrite markedly intensifies damage in LCF yet has no influence during slow-strain-rate tensile testing at temperatures where martensite formation is not favoured.

Table 2. Summary of tensile and low-cycle fatigue test results in air and hydrogen at different temperatures.

Testing mode	**Temperature (°C)**	**Environment**	**RRA**	**Normalized fatigue life (*N*)**
Tensile	RT	Air and H_2	0.37	—
Tensile	150	Air and H_2	0.91	—
LCF	RT	Air	—	1.00
LCF	RT	H_2	—	0.49
LCF	120	Air	—	1.56
LCF	120	H_2	—	0.54

Table 2 summarizes the results from mechanical testing. A relative reduction of area (RRA) value of 0.37 obtained from tensile testing at room temperature indicates significant hydrogen embrittlement. In contrast, the RRA increased to 0.91 at 150°C, suggesting that hydrogen embrittlement was almost entirely mitigated at this elevated temperature. This trend aligns with observations reported for AISI 304, where RRA values increase with temperature, indicating reduced susceptibility to hydrogen embrittlement at static conditions [14,47]. Table 2 also presents the number of cycles to crack initiation from LCF testing, normalized to the fatigue life at room temperature in air. A reduction in fatigue life is observed at both 120°C and room temperature when tested in hydrogen, confirming that hydrogen embrittlement persists under cyclic loading, at both temperatures.

LCF specimens tested in air at room temperature exhibit fatigue striations, whereas their hydrogen-charged counterparts show cleavage and secondary cracks (Fig. 8a). Energy dispersive spectroscopy reveals that these secondary cracks are associated with δ-ferrite, identified by chromium enrichment and nickel depletion at the crack interfaces (Fig. 8a-b). A similar trend is observed under monotonic loading. Tensile specimens fractured in hydrogen

exhibit transgranular cleavage with δ-ferrite cracking as shown in Fig. 8c-d, while reference tests performed in air show fatigue striations in LCF and dimples in tensile test, indicative of better ductility.

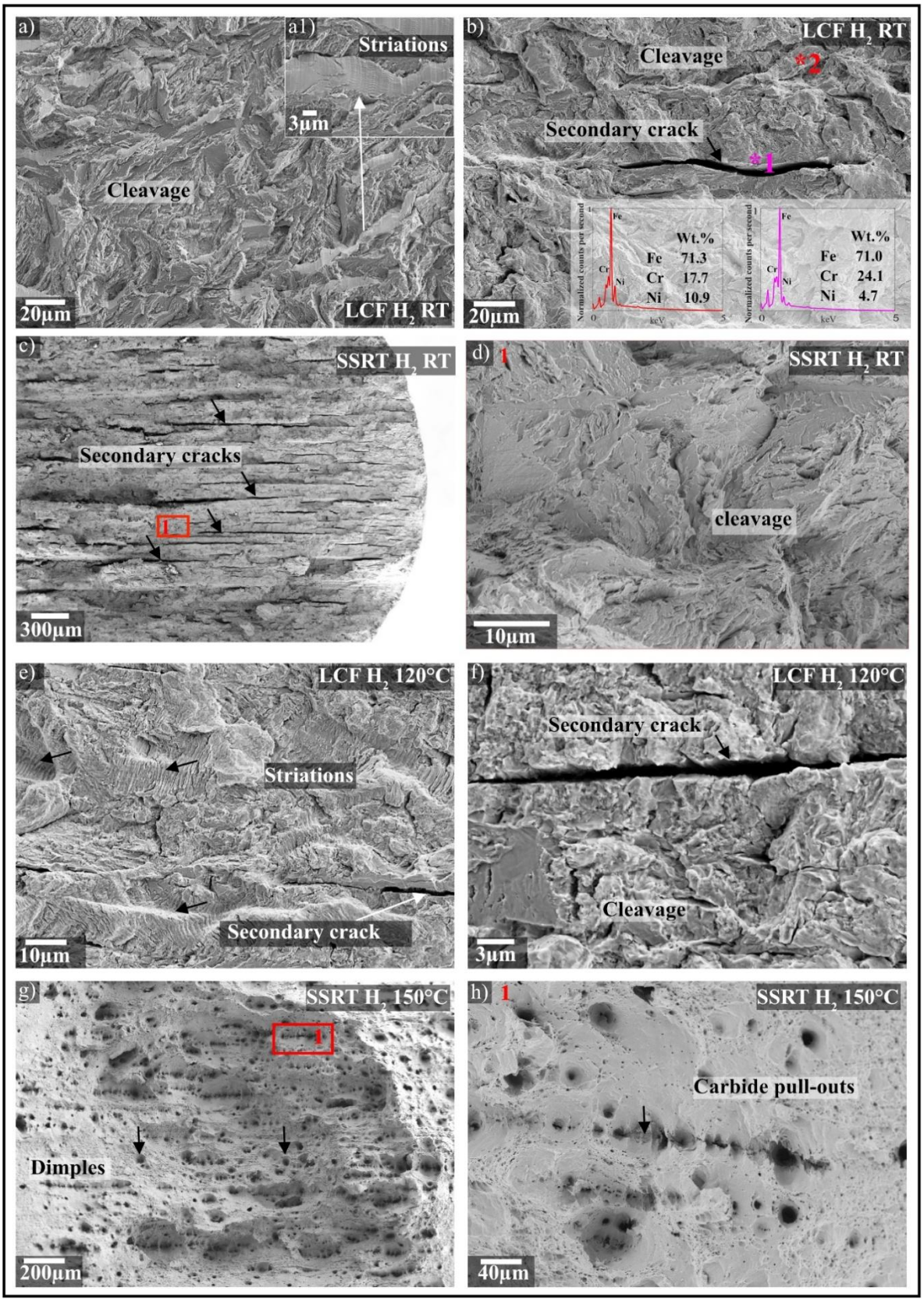

Fig. 8. Fracture surfaces after testing in hydrogen: (a–b) LCF at room temperature (RT), (c–d) tensile at RT, (e–f) LCF at 120°C, and (g-h) tensile at 150°C.

At elevated temperatures, 120°C for LCF and 150°C for tensile testing, the hydrogen effect differs. While HE is not observed in tensile testing at 150°C, pronounced embrittlement, comparable to room temperature, is seen in LCF at 120°C (see Table 2). Fracture surfaces of LCF specimens from testing at 120°C exhibit more zones of striations, and secondary cracks along δ-ferrite (Fig. 8e-f). In contrast, fracture surfaces from tensile tested specimens at 150°C retain a ductile appearance with dimple morphology and carbide pull-outs (Fig. 8g and Fig. 8h). The EBSD phase maps shown in Fig. 9a and Fig. 9b confirm the absence of martensite formation at 120°C and 150°C, respectively. It is evident that δ-ferrite influences HE susceptibility differently in LCF and tensile testing when martensite is absent. In the absence of DIM, the deformation of austenite progressed through slip in both tensile and LCF testing. The EBSD band contrast map shown in Fig. 10a depicts post-mortem microstructure of LCF specimen failed in hydrogen at 120°C. During LCF at 120°C, localized deformation at δ-ferrite phase boundaries is revealed by cECCI micrograph (Fig. 10b). This strain localization in the presence of hydrogen at these interfaces could lead to localization of deformation and can prevent crack tip blunting leading to accelerated propagation of cracks [11].

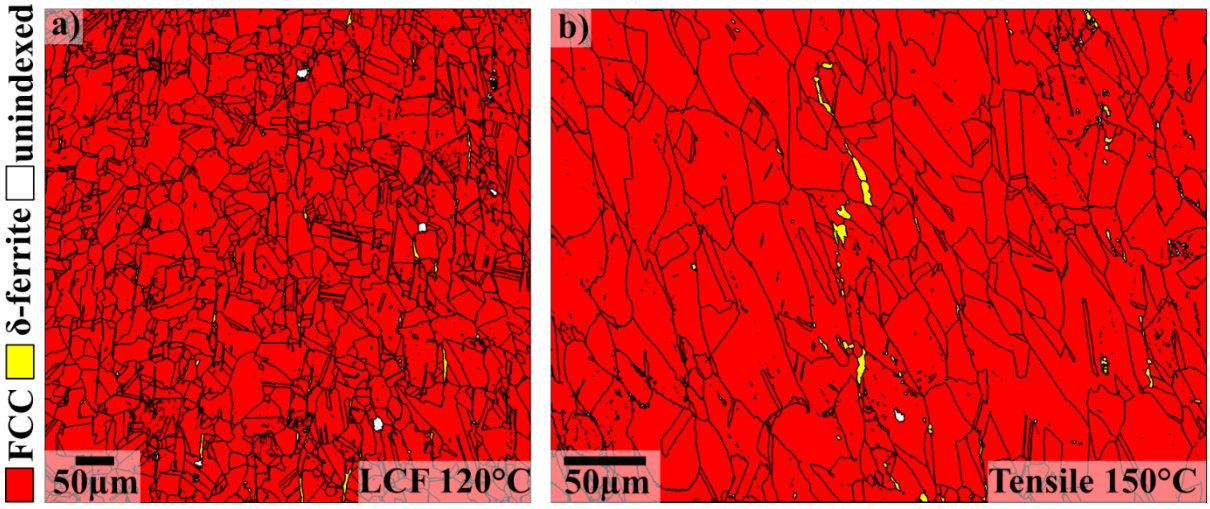

Fig. 9. EBSD phase map of (a) LCF specimen tested at 120°C in hydrogen; (b) tensile tested at 150°C in hydrogen.

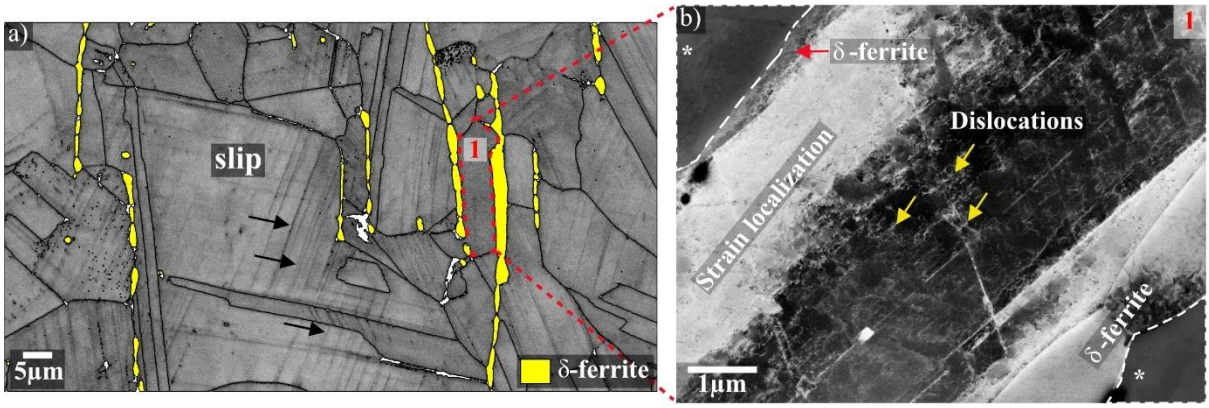

Fig. 10. (a) Band contrast image of LCF specimens tested at 120°C in hydrogen; (b) strain localization at delta-ferrite boundaries revealed using cECCI at site '1' marked in (a); grains marked with * are not oriented for cECCI.

The observed reduction in fatigue life at 120°C in hydrogen may be attributed to strain localization along δ-ferrite, which appears to promote crack formation more effectively in fatigue than in tensile testing. This is likely due to the distinct damage evolution mechanisms

in fatigue, which involve cyclic hardening/softening, saturation, followed by cyclic slip irreversibilities and localized deformation that ultimately lead to crack initiation and propagation [39]. In contrast, tensile testing subjects the material to more uniform global loading, and embrittlement typically requires the formation of martensite, as cleavage must occur across a substantial portion of the cross-sectional area to cause a measurable drop in ductility without necking. These findings highlight the critical role of δ-ferrite in hydrogen embrittlement under cyclic loading and underscore the importance of minimizing δ-ferrite content. Furthermore, the necessity of using both LCF testing and SSR tensile testing to comprehensively assess HE over a broad temperature range is demonstrated.

Effect of cyclic pre-deformation (Paper 3)

Paper 3 investigates the influence of cyclic pre-deformation on HE susceptibility through thermal hydrogen pre-charging followed by strain-controlled LCF testing under ambient atmospheric conditions. Cyclic pre-deformation (100 cycles), as illustrated in Fig. 11a, led to the formation of slip/shear bands at strain amplitude of 0.3%. Additionally, minimal martensite content was observed at 0.6% strain amplitude, as shown in Fig. 11b and Fig. 11c. Fatigue-induced dislocation cell structures were also evident at these strain levels, as presented in Fig. 11d and Fig. 11e.

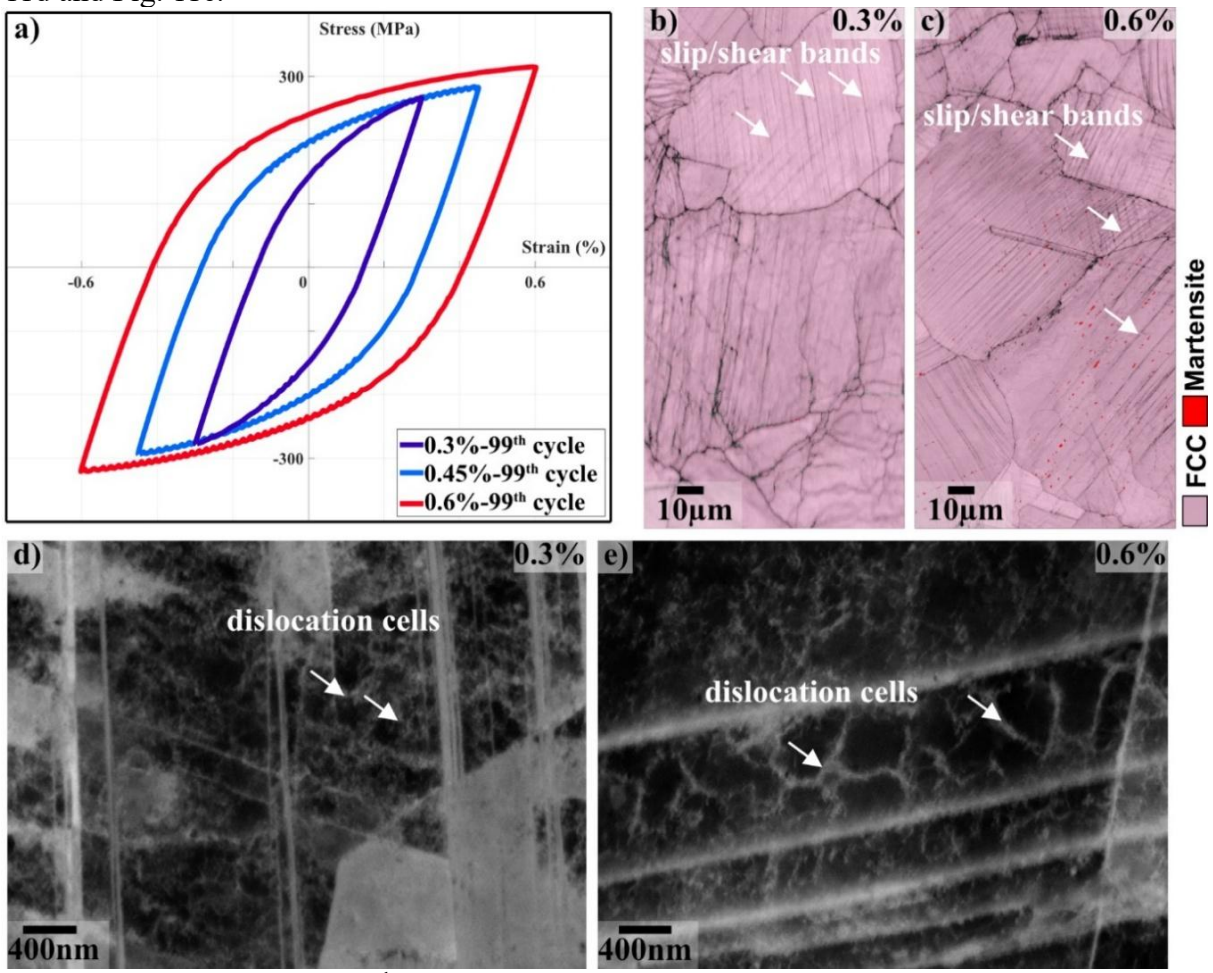

Fig. 11. (a) Fatigue hysteresis at 99th cycle; band contrast map overlaid with phase map showing slip/shear bands at strain amplitudes of (b) 0.3% and (c) 0.6%; (d) & (e) presence of dislocation cells at strain amplitudes of 0.3% and 0.6%, respectively.

Fatigue testing of pre-cycled and non-pre-cycled test bars with hydrogen pre-charging resulted in reduced fatigue life compared to their reference states tested without hydrogen pre-charging across all the tested strain amplitudes. Additionally, the pre-cycled test bars exhibited a distinct re-hardening stage, as shown in Fig. 12a, followed by cyclic softening. This re-hardening behaviour was unique to the pre-cycled test bars and is attributed to the thermal exposure. The re-hardening stage observed after prolonged thermal exposure (350°C for 28 days), could be due to static strain ageing of pre-deformed austenite. Note that partial dislocation rearrangement/annihilation during thermal exposure may have occurred beside static strain ageing. Despite the microstructural changes, the fatigue life of both pre-cycled and non-pre-cycled specimens remained comparable, as illustrated in Fig. 12b. The EBSD analysis confirmed the presence of BCC phase, expected to be martensite, and dislocations after thermal exposure, as seen in Fig. 13a and Fig. 13b.

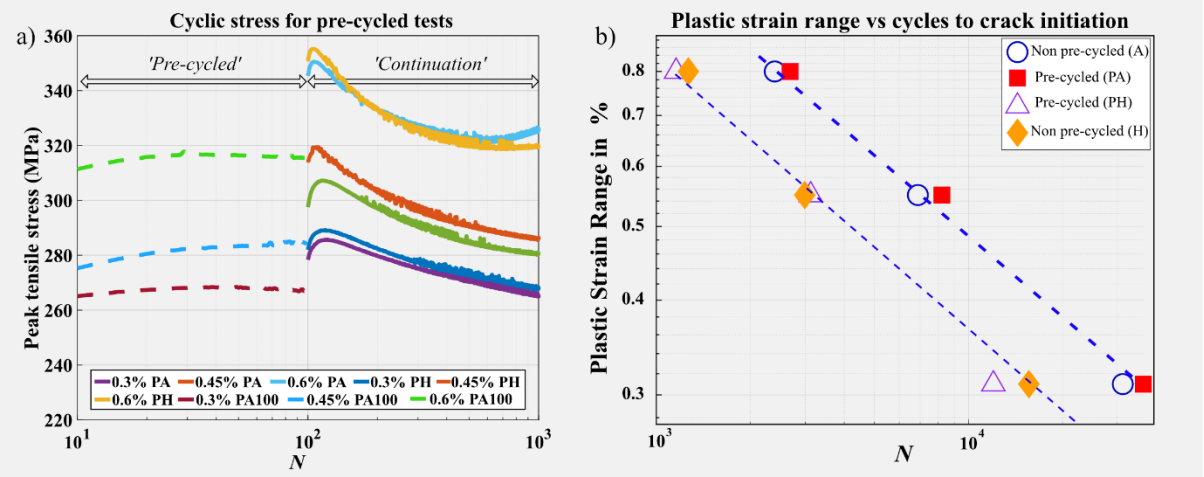

Fig. 12. (a) Cyclic stress response for pre-cycled test bars at different strain amplitudes, PA100: pre-cycled in air for 100 cycles; PA: precycled in air followed by thermal treatment in air prior to fatigue test; PH: pre-cycled in air followed by thermal hydrogen charging prior to fatigue test (b) plastic strain range vs cycles to crack initiation (*N*), here A: no hydrogen pre-charging, H: with hydrogen pre-charging.

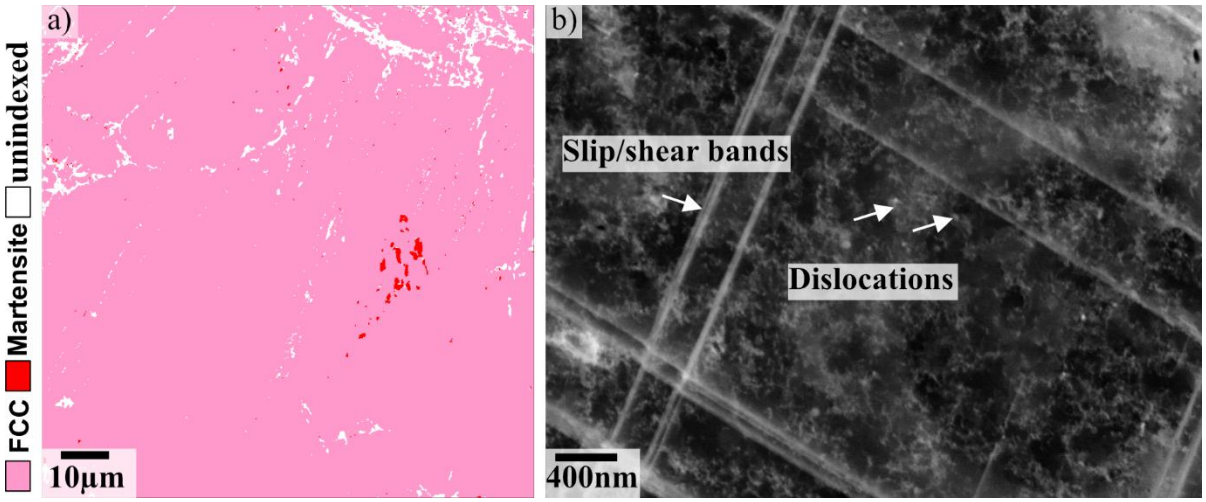

Fig. 13. (a) EBSD phase map from the test bar with pre-cycling at 0.6% strain amplitude and thermally exposed at 350°C for 28 days, showing presence of BCC phase expected to be martensite; (b) ECCI micrograph from the same sample showing dislocations and slip/shear bands.

Due to similarities between fracture surfaces in pre-cycled and non-pre-cycled states, only fracture surfaces of pre-cycled test bars at selected strain amplitudes are presented in Fig. 14. For specimens tested without hydrogen pre-charging, typical fatigue features such as striations and cracking of Ti(C,N) precipitates are observed across all tested strain amplitudes, as shown in Fig. 14a-b. In contrast, pre-cycled test bars with subsequently charged hydrogen exhibit a noticeable reduction in fatigue life, which is reflected in the fracture morphology. A mix of ductile and brittle fracture features are observed, comprising regions of fatigue striations indicative of ductility and cleavage typical of brittle fracture, as shown in Fig. 14c. Additionally, secondary cracking and Ti(C,N) precipitate fracture are evident in Fig. 14d. Given the similarity in fracture surface features across hydrogen pre-charged conditions, only results at 0.45% strain amplitude are presented. The observed fracture behaviour can be attributed to DIM formation. Since hydrogen solubility in martensite is lower than in austenite, hydrogen tends to supersaturate and accumulate at martensite-austenite interfaces. During loading, these hydrogen-enriched interfaces become embrittled, promoting crack initiation and propagation [10]. As DIM formation is non-uniform, the shift in crack path may explain the observed striation patterns, as austenite is relatively resistant to hydrogen embrittlement. Furthermore, the relatively low δ-ferrite content (compared to that reported in Paper 1) and the distinct testing conditions may contribute to the presence of this mix fracture morphology with qualitatively more regions with striations at RT.

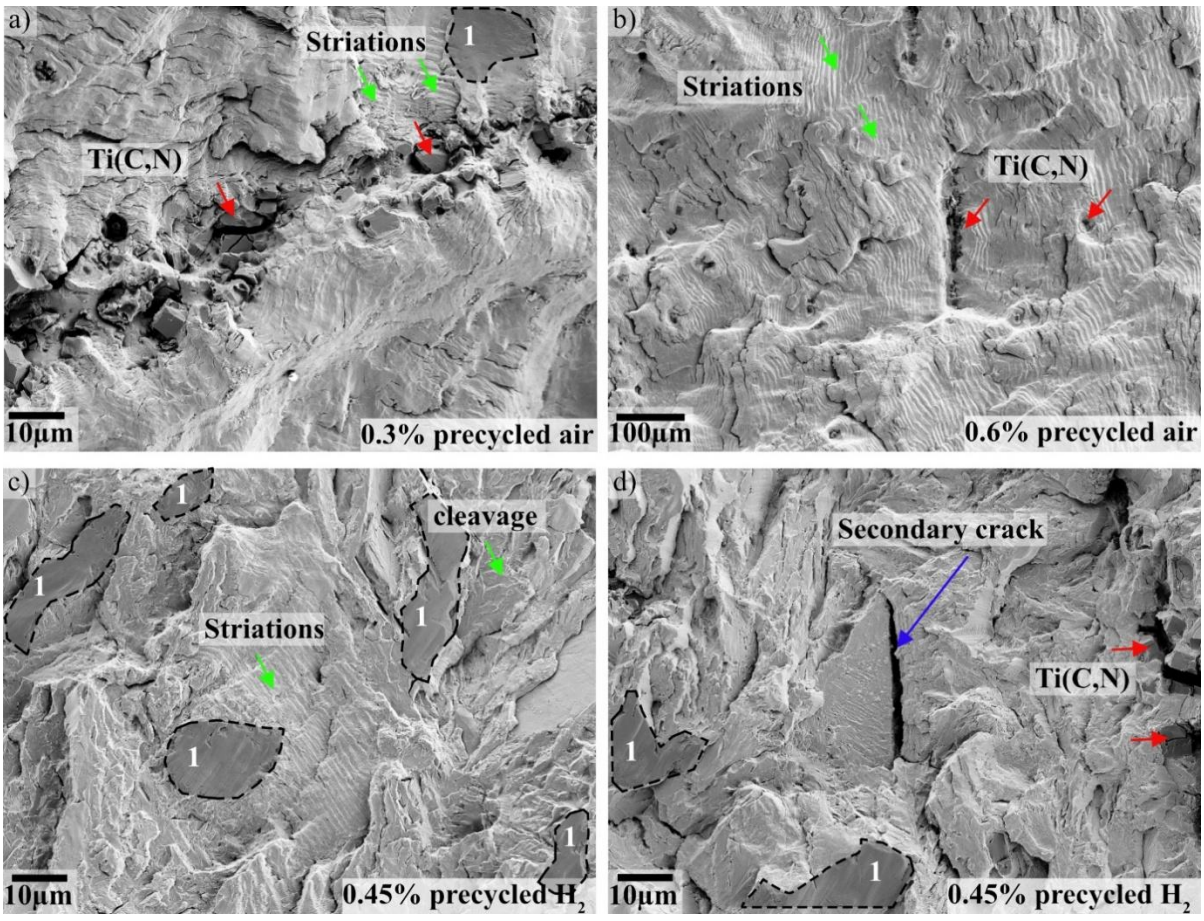

Fig. 14. (a) Fracture surface of pre-cycled specimens without hydrogen pre-charging at strain amplitude of (a) 0.3% and (b) 0.6%; (c) & (d) shows the fracture surfaces of pre-cycled test bars with pre-charged hydrogen at strain amplitude of 0.45%; regions marked as '1' refers to damage induced from fracture surface mating.

Overall, the effect of pre-cycling on LCF life was insignificant, primarily due to the limited martensite formation during pre-cycling and the use of prolonged hydrogen pre-charging at the elevated temperature, which likely led to saturation conditions. These findings support the adoption of simplified testing procedures where hydrogen pre-charging to near saturation levels is achieved prior to LCF testing. This approach serves as a practical approximation of industrially relevant loading conditions for gas turbines, which involve continuous hydrogen exposure during load cycles and extended hold periods.

7 Conclusions

Based on the work presented in this thesis, the following conclusions can be drawn:

Research question 1: How do temperature and loading mode affect hydrogen embrittlement in AISI 321 stainless steel?

1. Hydrogen embrittlement was observed at room temperature in both loading modes investigated, i.e., tensile and LCF.
2. Hydrogen embrittlement remained pronounced at 120°C during strain-controlled low-cycle, despite the absence of deformation-induced martensite. Fracture surfaces at this temperature exhibited secondary cracking along δ-ferrite phase boundaries as seen in their room temperature counterparts.
3. Strain localization along the δ-ferrite/austenite phase boundaries in the presence of hydrogen appears sufficient to initiate and propagate fatigue cracks, contributing to reduced fatigue life.
4. Under slow strain rate tensile testing, no evidence of hydrogen embrittlement was observed at 150°C. Fracture surfaces at this temperature showed ductile features such as dimples and Ti(C,N) precipitate pull-outs. In contrast, tensile specimens tested at room temperature exhibited transgranular cleavage and secondary cracking along δ-ferrite interfaces.

These findings highlight the influence of both loading mode and temperature on hydrogen embrittlement susceptibility. The absence of embrittlement in tensile tests at elevated temperatures is attributed to the nature of monotonic deformation, where martensite transformation appears necessary to embrittle a sufficient cross-sectional area. In contrast, LCF imposes more localized loading, making it more sensitive to interface-related damage.

Research question 2: Is the sequence of plastic deformation and hydrogen pre-charging affecting hydrogen embrittlement susceptibility in AISI 321 stainless steel?

1. Cyclic pre-deformation spanning 100 cycles, resulted in the formation of slip/shear bands at all tested strain amplitudes, while deformation-induced martensite formation was minimal at strain amplitude of 0.6%.
2. Pre-cycled specimens exhibited a re-hardening response upon test continuation, independent of hydrogen pre-charging. This may be due to static strain ageing and partial dislocation rearrangement/annihilation from the 28-day thermal exposure at 350°C.
3. The fatigue life remained similar in both pre-cycled and non-precycled state, both with and without hydrogen pre-charging.
4. The negligible impact of pre-cycling on fatigue performance can be attributed to two factors: the limited martensite content resulting from cyclic pre-deformation and the pre-charging conditions that likely led to hydrogen saturation.

The insignificant difference between fatigue lives in pre-cycled and non-pre-cycled conditions supports the adoption of simplified testing procedures in conditions that approach hydrogen

saturation before LCF testing, as a practical approximation of service conditions involving continuous hydrogen exposure during cyclic loading and prolonged hold times, like that of a gas turbine.

Future Work

Dry low emission (DLE) burners is a vital component in gas turbines, which enables lean premixing of hydrogen which results in significant reduction of NO_x emissions. The design flexibility of powder bed fusion laser beam (PBF-LB) additive manufacturing allows for manufacturing of intricate internal channels that facilitate improved fuel-air mixing in such components.

In these components, during start-up and shut down events of the gas turbine, the main loading is strain-driven, inducing significant inelastic deformations. This coupled with temperature variations through the cycle, makes thermomechanical fatigue the dominant mode of failure. The increasing solubility and diffusivity of hydrogen with temperature create a hydrogen uptake cycle for components in hydrogen-fuelled gas turbines. However, thermomechanical fatigue testing capability in hydrogen gas is limited, making it an underexplored area of research.

To address this challenge, it is essential to evaluate hydrogen embrittlement under service-like conditions. Future work will focus on characterization of AISI 321, and PBF-LB Hastelloy X subjected to thermomechanical fatigue testing in hydrogen gas. Fatigue crack propagation studies for Hastelloy X in hydrogen gas are also to be performed.

Acknowledgements

I am grateful to Prof. Emmy Yu Cao, Prof. Johan Ahlström, and Prof. Lars Nyborg for their valuable supervision, guidance, and insights during my thesis work at Chalmers University of Technology. I would like to thank Prof. Uta Klement, head of division Materials and Manufacture for her support.

This study was performed within the framework of the TechForH2 competence centre supported by Swedish Energy Agency, Chalmers University of Technology and industrial partners.

In this context, I would like to sincerely acknowledge Siemens Energy, particularly Frans Palmert, Stefan Wanjura, and Dirk Kulawinski, for their active involvement in the project and for providing industrial supervision and support throughout the work.

Thanks to Dr. Antonio Mulone for his assistance with microscopy and sample preparation.

Thank you to my friends and colleagues in the Department of Industrial and Materials Science for their support and insightful feedback.

References

[1] E. Stefan, B. Talic, Y. Larring, A. Gruber, T.A. Peters, Materials challenges in hydrogen-fuelled gas turbines, Int. Mater. Rev. 67 (2022) 461–486. https://doi.org/10.1080/09506608.2021.1981706.

[2] S.M. Kumar, N.S. Shanmugam, Studies on the weldability , mechanical properties and microstructural characterization of activated flux TIG welding of AISI 321 austenitic stainless steel Studies on the weldability , mechanical properties and microstructural characterization of activat, (n.d.).

[3] H. Yu, X. Lu, B. Sun, Y. Ding, M. Koyama, J. He, X. Zhou, A. Oudriss, X. Feaugas, Z. Zhang, Hydrogen Embrittlement as a Conspicuous Material Challenge Comprehensive Review and Future Directions, (n.d.). https://doi.org/10.1021/acs.chemrev.3c00624.

[4] H.C. Alloys, A.S. Steel, F. Steel, J. Jürgensen, A. Frehn, K. Ohla, S. Stolz, Effect of Hydrogen Charging on the Mechanical Properties of High-Strength Copper-Base Alloys, Austenitic Stainless Steel AISI 321, Inconel 625 and Ferritic Steel 1.4511, (2024).

[5] A.I. Mourad, S. Sajith, S. Shitole, A. Almomani, S.H. Khan, A. Elsheikh, A. Kareem, Fatigue life and crack growth prediction of metallic structures : A review, Structures 76 (2025) 109031. https://doi.org/10.1016/j.istruc.2025.109031.

[6] Y.S. Kim, S.H. Bak, S.S. Kim, Effect of Strain-Induced Martensite on Tensile Properties and Hydrogen Embrittlement of 304 Stainless Steel, Metall. Mater. Trans. A Phys. Metall. Mater. Sci. 47 (2016) 222–230. https://doi.org/10.1007/s11661-015-3198-4.

[7] X. Qin, L. Nyborg, H. Liu, A. Bauer, Y. Cao, Low-temperature carburizing improves hydrogen embrittlement resistance of cold worked 304 austenitic stainless steel, J. Mater. Res. Technol. 36 (2025) 8816–8825. https://doi.org/10.1016/j.jmrt.2025.05.125.

[8] J.R. Buckley, D. Hardie, The effect of pre-straining and δ-ferrite on the embrittlement of 304L stainless steel by hydrogen, Corros. Sci. 34 (1993) 93–107. https://doi.org/10.1016/0010-938X(93)90261-E.

[9] X. Xiuqing, A. Junwei, W. Chen, N. Jing, Study on the hydrogen embrittlement susceptibility of AISI 321 stainless steel, Eng. Fail. Anal. 122 (2021) 105212. https://doi.org/10.1016/j.engfailanal.2020.105212.

[10] K.E. Nygren, A. Nagao, P. Sofronis, I.M. Robertson, The Role of Microstructure in Hydrogen-Induced Fatigue Failure of 304 Austenitic Stainless Steel, Metall. Mater. Trans. A Phys. Metall. Mater. Sci. 51 (2020) 5704–5714. https://doi.org/10.1007/s11661-020-05977-w.

[11] F. Bao, K. Zhang, Z. Zhou, W. Zhang, X. Cai, L. Zhang, Effect of δ-ferrite on susceptibility to hydrogen embrittlement of 304 austenitic stainless steel in high-pressure hydrogen atmosphere, Anti-Corrosion Methods Mater. 68 (2021) 202–208. https://doi.org/10.1108/ACMM-11-2020-2403.

[12] A. Jain, A. Varshney, A critical review on deformation-induced transformation

kinetics of austenitic stainless steels, Mater. Sci. Technol. (United Kingdom) 40 (2024) 75–106. https://doi.org/10.1177/02670836231212618.

[13] M. Grosse, D. Kalkhof, M. Niffenegger, L. Keller, Influencing parameters on martensite transformation during low-cycle fatigue for steel AISI 321, 437 (2006) 109–113. https://doi.org/10.1016/j.msea.2006.04.077.

[14] J.A. Lee, Hydrogen Embrittlement. NASA/TM-2016–218602, Shreir's Corros. (2016) 1–62. https://ntrs.nasa.gov/api/citations/20160005654/downloads/20160005654.pdf.

[15] W.W. Yanfei Wang, Xuanpei Wu, Effect of α Martensite Content Induced by Tensile Plastic Prestrain on Hydrogen Transport and Hydrogen, (2018). https://doi.org/10.3390/met8090660.

[16] Y. Wang, X. Wang, J. Gong, L. Shen, ScienceDirect Hydrogen embrittlement of catholically hydrogen-precharged 304L austenitic stainless steel : Effect of plastic pre-strain, Int. J. Hydrogen Energy 39 (2014) 13909–13918. https://doi.org/10.1016/j.ijhydene.2014.04.122.

[17] A.T. Gee, B.E. Hayden, C. Mormiche, T.S. Nunney, The role of steps in the dynamics of hydrogen dissociation on Pt(533), J. Chem. Phys. 112 (2000) 7660–7668. https://doi.org/10.1063/1.481360.

[18] W.H. Johnson, W. Thomson, On some remarkable changes produced in iron and steel by the action of hydrogen and acids, Proc. R. Soc. London 23 (1875) 168–179. https://doi.org/10.1098/rspl.1874.0024.

[19] M.Y. Demeri, 10.5 Formability of Austenitic Stainless Steels, Adv. High-Strength Steels - Sci. Technol. Appl. (2013). https://app.knovel.com/hotlink/khtml/id:kt00U5KPK1/advanced-high-strength/formability-austenitic.

[20] Y. Yin, R. Faulkner, F. Starr, 5 - Austenitic steels and alloys for power plants, in: A. Shirzadi, S. Jackson (Eds.), Struct. Alloy. Power Plants, Woodhead Publishing, 2014: pp. 105–152. https://doi.org/https://doi.org/10.1533/9780857097552.2.105.

[21] G. George, H. Shaikh, 1 - Introduction to Austenitic Stainless Steels, in: H.S. Khatak, B. Raj (Eds.), Corros. Austenitic Stainl. Steels, Woodhead Publishing, 2002: pp. 1–36. https://doi.org/https://doi.org/10.1533/9780857094018.37.

[22] M. Türker, A.T. Ertürk, E. Karakulak, E.A. Güven, Effects of Different Heat Treatments on Microstructure, Toughness and Wear Behavior of G-X 10CrNiMoNb 18-10 Cast Austenitic Stainless Steel, Trans. Indian Inst. Met. 71 (2018) 1033–1040. https://doi.org/10.1007/s12666-017-1238-z.

[23] British Stainless Steel Association, Magnetic Properties of Stainless Steel - SSAS Information Sheet No.2.81, 304 (2000) 1–2. http://www.bssa.org.uk/cms/File/SSAS2.81-Magnetic Properties.pdf.

[24] B. Rafiei, B.M. Sadeghi, B. Mirzakhani, Y. Payandeh, F. Rahimi, Transformation-Induced Plasticity in 304 and 304L Stainless Steels and Its Effect on Tensile Behavior and Anisotropy, J. Mater. Eng. Perform. (2024) 18–20. https://doi.org/10.1007/s11665-024-09478-4.

[25] A.A. Tiamiyu, A.G. Odeshi, J.A. Szpunar, Deformation and strengthening mechanisms in AISI 321 austenitic stainless steel under both dynamic and quasi-static loading

conditions, Miner. Met. Mater. Ser. Part F6 (2017) 191–202. https://doi.org/10.1007/978-3-319-51493-2_19.

[26] S. Ooi, P.H.K.D.H. Bhadeshia, Hydrogen in Austenite: What Changes after Martensitic Transformation? Shengda Pu, (2018).

[27] R. Naraghi, A. Borgenstam, Martensitic Transformation in Austenitic Stainless Steels Reza Naraghi, (2016).

[28] P. Rozenak, Effects of nitrogen on hydrogen embrittlement in AISI type 316, 321 and 347 austenitic stainless steels, 25 (1990).

[29] P. Rozenak, D. Eliezer, Effects of metallurgical variables on hydrogen embrittlement in AISI type 316, 321 and 347 stainless steels, Mater. Sci. Eng. 61 (1983) 31–41. https://doi.org/10.1016/0025-5416(83)90123-4.

[30] H.S. Yun, S.K. Jeon, Y.K. Lee, J.S. Park, S.H. Nahm, Effect of precharging methods on the hydrogen embrittlement of 304 stainless steel, Int. J. Hydrogen Energy 50 (2024) 175–188. https://doi.org/10.1016/j.ijhydene.2023.09.073.

[31] C.S. Marchi, T. Michler, K.A. Nibur, B.P. Somerday, On the physical differences between tensile testing of type 304 and 316 austenitic stainless steels with internal hydrogen and in external hydrogen, Int. J. Hydrogen Energy 35 (2010) 9736–9745. https://doi.org/10.1016/j.ijhydene.2010.06.018.

[32] Y. Murakami, T. Kanezaki, Y. Mine, S. Matsuoka, Hydrogen embrittlement mechanism in fatigue of austenitic stainless steels, Metall. Mater. Trans. A Phys. Metall. Mater. Sci. 39 A (2008) 1327–1339. https://doi.org/10.1007/s11661-008-9506-5.

[33] T. Kanezaki, C. Narazaki, Y. Mine, S. Matsuoka, Y. Murakami, Effects of hydrogen on fatigue crack growth behavior of austenitic stainless steels, Int. J. Hydrogen Energy 33 (2008) 2604–2619. https://doi.org/10.1016/j.ijhydene.2008.02.067.

[34] D. Choi, J. Nam, B. Moon, S.K. Saha, J. Yoo, J.M. Park, K.H. Yun, N. Kang, Effect of δ–ferrite and strain-induced martensite on hydrogen embrittlement of STS 308 L and STS 316 L all-weld metals, Corros. Sci. 231 (2024) 111977. https://doi.org/10.1016/j.corsci.2024.111977.

[35] G.B. Rawls, T. Adams, N.L. Newhouse, Hydrogen production and containment, Gaseous Hydrog. Embrittlement Mater. Energy Technol. Probl. Its Characterisation Eff. Part. Alloy Classes (2012) 3–50. https://doi.org/10.1533/9780857093899.1.3.

[36] www. astm. org. 3 ASTM G129-00. Standard Practice for Slow Strain Rate Testing to Evaluate the Susceptibility of Metallic Materials to Environmentally Assisted Cracking, ASTM International, West Conshohocken, PA, 2000 (R 2013), iTeh Standards iTeh Standards, 00 (2021) 2–3. https://doi.org/10.1520/G0129-00R13.10.1520/G0129-21.2.

[37] N.E. Dowling, Mechanical behavior of materials: engineering methods for deformation, fracture, and fatigue, Pearson Education, 2012.

[38] C. Izawa, S. Wagner, M. Deutges, M. Martín, S. Weber, R. Pargeter, T. Michler, H.H. Uchida, R. Gemma, A. Pundt, Relationship between hydrogen embrittlement and Md30 temperature: Prediction of low-nickel austenitic stainless steel's resistance, Int. J. Hydrogen Energy 44 (2019) 25064–25075.

https://doi.org/10.1016/j.ijhydene.2019.07.179.

[39] H. Mughrabi, Microstructural mechanisms of cyclic deformation, fatigue crack initiation and early crack growth, Philos. Trans. R. Soc. A Math. Phys. Eng. Sci. 373 (2015). https://doi.org/10.1098/rsta.2014.0132.

[40] J. Coffin L. F., A Study of the Effects of Cyclic Thermal Stresses on a Ductile Metal, Trans. Am. Soc. Mech. Eng. 76 (2022) 931–949. https://doi.org/10.1115/1.4015020.

[41] H. Vehoff, 6 . Hydrogen Related Material Problems, 73 (1997).

[42] L.C. FRITZEMEIER, W.T. CHANDLER, Hydrogen Embrittlement—Rocket Engine Applications, ACADEMIC PRESS, INC., 1989. https://doi.org/10.1016/b978-0-12-690845-9.50021-x.

[43] M. Martin, S. Weber, C. Izawa, S. Wagner, A. Pundt, W. Theisen, Influence of machining-induced martensite on hydrogen-assisted fracture of AISI type 304 austenitic stainless steel, Int. J. Hydrogen Energy 36 (2011) 11195–11206. https://doi.org/10.1016/j.ijhydene.2011.05.133.

[44] T. Michler, J. Naumann, M. Hock, K. Berreth, M.P. Balogh, E. Sattler, Microstructural properties controlling hydrogen environment embrittlement of cold worked 316 type austenitic stainless steels, Mater. Sci. Eng. A 628 (2015) 252–261. https://doi.org/10.1016/j.msea.2015.01.054.

[45] S. Zaefferer, N.N. Elhami, Theory and application of electron channelling contrast imaging under controlled diffraction conditions, Acta Mater. 75 (2014) 20–50. https://doi.org/10.1016/j.actamat.2014.04.018.

[46] F. Bachmann, R. Hielscher, H. Schaeben, Texture Analysis with MTEX – Free and Open Source Software Toolbox, Solid State Phenom. 160 (2010) 63–68. https://doi.org/10.4028/www.scientific.net/SSP.160.63.

[47] C. Marchi, Technical Reference on Hydrogen Compatibility of Materials. Austenitic Stainless Steels, 304, Lab. Sandia Natl. (2005) 1–18.